Lidar detection of high concentrations of ozone and aerosol transported from Northeast Asia over Saga, Japan

Osamu Uchino[1, 2], Tetsu Sakai[2], Toshiharu Izumi[2], Tomohiro Nagai[2], Isamu Morino[1], Akihiro Yamazaki[2], Makoto Deushi[3], Keiya Yumimoto[2], Takashi Maki[2], Taichu Y. Tanaka[2], Taiga Akaho[4], Hiroshi Okumura[4], Kohei Arai[4], Takahiro Nakatsuru[1], Tsuneo Matsunaga[1], Tatsuya Yokota[1]

[1]National Institute for Environmental Studies, 16-2 Onogawa, Tsukuba, Ibaraki 305-8506, Japan
[2]Meteorological Research Institute, 1-1 Nagamine, Tsukuba, Ibaraki 305-0052, Japan
[3]Japan Meteorological Agency, 1-3-4 Otemachi, Chiyoda-ku, Tokyo 100-8122, Japan
[4]Saga University, 1 Honjou, Saga, Saga 840-8502, Japan

Correspondence to: O. Uchino (uchino.osamu@nies.go.jp)

Abstract. To validate products of the Greenhouse gases Observing SATellite (GOSAT), we observed vertical profiles of aerosols, thin cirrus clouds, and tropospheric ozone with a mobile lidar system that consisted of a two-wavelength (532 and 1064 nm) polarization lidar and a tropospheric ozone Differential Absorption Lidar (DIAL). We used these lidars to make continuous measurements over Saga (33.24°N, 130.29°E) during 20–31 March 2015. High ozone and high aerosol concentrations were observed almost simultaneously in the altitude range 0.5–1.5 km from 03:00 to 20:00 Japan Standard Time on 22 March 2015. The maximum ozone volume mixing ratio was ~110 ppbv. The maxima of the aerosol extinction coefficient and optical depth at 532 nm were 1.2 km^{-1} and 2.1, respectively. Backward trajectory analysis and the simulations by the Model of Aerosol Species IN the Global AtmospheRe (MASINGAR) mk-2 and the Meteorological Research Institute Chemistry-Climate Model, version 2 (MRI-CCM2) indicated that mineral dust particles from the Gobi Desert and an air mass with high ozone and aerosol (mainly sulfate) concentrations that originated from the North China Plain could have been transported over the measurement site within about two days. These high ozone and aerosol concentrations impacted surface air quality substantially in the afternoon of 22 March 2015. After some modifications of its physical and chemical parameters, MRI-CCM2 approximately reproduced the high-ozone volume-mixing ratio. The MASINGAR mk-2 successfully predicted high aerosol concentrations, but the predicted peak aerosol optical thickness was about one-third of the observed value.

1 Introduction

Tropospheric ozone is a major air pollutant and impacts human health and vegetation (HTAP, 2010; Yue and Unger, 2014). It is also an important greenhouse gas (IPCC, 2013). Tropospheric aerosols are also air pollutants and aggravate respiratory conditions (HTAP, 2010). Tropospheric aerosols also enhance radiative forcing in a negative (sulfuric acid particles) or positive (black carbon) way (IPCC, 2013), and they affect remote sensing such as the measurement of greenhouse gases from space (Houweling et al., 2005; Uchino et al., 2012a). It is therefore very important to monitor tropospheric ozone and aerosols and to understand their temporal and spatial variations. On the one hand, aerosols transported from East Asia to western Japan have been observed by lidar, and their vertical distributions have been reported (Iwasaka et al., 1988: Murayama et al., 2001; Hara et al., 2009). On the other hand, ozone from Asia has been studied mainly via surface measurements (Akimoto et al., 1996; Yamaji et al., 2006). Continuous ozone vertical distributions measured by DIfferential Absorption Lidar (DIAL) are very useful for studying transport processes and the origin of the ozone.

To validate products of the Greenhouse gases Observing SATellite (GOSAT), we developed a two-wavelength (532 and 1064 nm) polarization lidar (hereafter abbreviated as Mie lidar) to observe vertical profiles of tropospheric and stratospheric aerosols and thin cirrus clouds at the National Institute for Environmental Studies (NIES), Tsukuba (36.05°N, 140.13°E), Japan in 2009. In 2010 we also developed a DIAL to measure tropospheric ozone profiles (hereafter abbreviated as ozone DIAL). The ozone DIAL was installed in a container with the Mie lidar. In March 2011, we moved the lidar container to Saga (33.24°N, 130.29°E) in the Kyushu district of western Japan at a location 2.6 m above sea level. The ozone DIAL was modified in September 2012 (Uchino et al., 2014).

Mie lidar has been used to demonstrate the influence of high-altitude aerosols and cirrus clouds on the GOSAT product of the column-averaged dry air mole fraction of carbon dioxide (XCO_2) retrieved from the Thermal And Near infrared Sensor for carbon Observation-Fourier Transform Spectrometer (TANSO-FTS) Short-Wavelength InfraRed (SWIR) spectral data onboard GOSAT. The XCO_2 data were improved by taking the vertical profiles of aerosols and cirrus clouds measured by Mie lidar into account (Uchino et al., 2012a). The increases of stratospheric aerosols caused by the 2009 Sarychev eruption and the 2011 Nabro eruption were observed by Mie lidar (Uchino et al., 2012b).

Ozone DIAL has been used to validate the GOSAT ozone product retrieved from TANSO-FTS Thermal InfraRed (TIR) spectral data (Ohyama et al., 2012), to observe ozone concentrations in the lower troposphere, and to compare the observed concentrations with those predicted by the Meteorological Research Institute Chemistry-Climate Model, version 2 (MRI-CCM2) (Deushi and Shibata, 2011). Use of Mie lidar and ozone DIAL will facilitate satellite product validation not only for GOSAT but also for upcoming satellites such as the TROPOspheric Monitoring Instrument (TROPOMI, Veefkind et al., 2012) and the Geostationary Environment Monitoring Spectroscopy (GEMS, Bak et al., 2013). High ozone episodes in the lower troposphere have been observed by lidar (Banta et al., 1998; Koutidis et al., 2002; Ancellet et al., 2005; Eisele and Trickl, 2005; Kuang et al., 2011). Those observational records were

limited to at most one week. We made an 11-day continuous record during 20–31 March 2015.

In this paper we report an event during which high concentrations of ozone and aerosols were observed almost simultaneously below an altitude of 1.5 km over Saga on 22 March 2015 by Mie lidar and ozone DIAL. That event substantially impacted surface air quality. We also compared the observational results with those simulated by the models.

2 Characteristics of the lidar system and observed parameters

Mie lidar and ozone DIAL were installed in a container with dimensions of about 228 cm (width), 683 cm (length), and 255 cm (height), as shown in Fig. 1. Mie lidar is a two-wavelength (532 and 1064 nm) polarization lidar based on a neodymium-doped yttrium-aluminum-garnet (Nd:YAG) laser; the characteristics are summarized in Table 1. The output energy at 532 and 1064 nm was 130 mJ, with a pulse repetition rate of 10 Hz. The diameter of the receiving telescope was 30.5 cm. The output signals from the photomultiplier tubes (PMT) and a silicon avalanche photodiode (APD) were processed by transient recorders with a 12-bit analog/digital converter and a photon counter.

The data analysis methods of Mie lidar and ozone DIAL have been described by Uchino et al. (2012b) and Uchino et al. (2014), respectively. We summarize the observation parameters obtained by Mie lidar. The backscattering ratio R is defined as

$$R = (BR + BA)/BR, \quad (1)$$

where BR and BA are the Rayleigh and Mie backscattering coefficients, respectively. Backscattering ratio profiles were derived by the inversion method (Fernald, 1984). The reference altitude was usually set between 9 and 12 km, where only molecular backscattering could be assumed in the absence of clouds. We assumed the lidar ratio LR (extinction-to-backscatter ratio) for aerosols to be 50 sr at 532 nm and 45 sr at 1064 nm based on the lidar ratios for Asian dust and pollutant aerosols summarized by Sakai et al. (2003), Anderson et al. (2003), and Cattrall et al. (2005). The following is a summary of their lidar ratios at 532 nm:

- Asian dust 47 ± 18 sr (Sakai et al., 2013);
- dust (spheroids) 42 ± 4 sr, Southeast Asia pollution 58 ± 10 sr (Cattral et al., 2005);
- ACE-Asia pollution (fine-dominated, submicron portion) 50 ± 5 sr, dust (coarse-dominated, dust-like chemistry, super-micron portion) 46 ± 8 sr (Anderson et al., 2003).

As a simplification, we used the same value for both Asian dust and pollutant aerosols. To calculate BR, we used the atmospheric molecular density profiles obtained by operational radiosondes at the Fukuoka District Meteorological Observatory (33.58°N, 130.38°E), Japan Meteorological Agency (JMA). The aerosol extinction coefficient was calculated by multiplying BA by LR.

The total volume depolarization ratio D was defined as

$$D = S / (P + S) \cdot 100\ (\%), \quad (2)$$

where P and S are the parallel and perpendicular components of the backscattered signals, respectively. The particle depolarization ratio D_p was obtained from the equation

$$D_p = (D \cdot R - D_m)/(R - 1), \quad (3)$$

where D_m is the atmospheric molecular depolarization ratio. We used a D_m value of 0.37% for this lidar system; we calculated D_m from the spectral transmission data of the interference filter at 532 nm and the Rayleigh backscattering cross sections (Sakai et al., 2003). The value of D_p indicates whether the particles are spherical or non-spherical; large values indicate the presence of non-spherical particles. The backscatter-related Ångström exponent *Alp*, the qualitative indicator of aerosol particle size, is defined by

$$BA(\lambda) \propto \lambda^{-Alp}, \quad (4)$$

where λ is the wavelength. Larger values of *Alp* indicate the predominance of smaller (i.e., submicrometer-sized) particles. The vertical resolution of these observational parameters was 150 m, and the time resolution was set to be 1 h for comparison with the Model of Aerosol Species in the Global Atmosphere (MASINGAR)-mk2 (Yukimoto et al., 2012). The lowest altitude of Mie lidar measurement was 225 m due to the imperfect overlap of the transmitter-receiver optical axes of the lidar system.

The ozone DIAL consisted of a Nd:YAG laser and a 2-m-long Raman cell filled with CO_2 gas that generated four Stokes lines from stimulated Raman scattering by CO_2 ; the characteristics are summarized in Table 2. In this study, we used three Stokes lines (276, 287, and 299 nm). The output energies of these Stokes lines were about 8–9 mJ per pulse, with a pulse repetition rate of 10 Hz. The receiving telescope diameters were 10 cm for boundary layer ozone measurements and 49 cm for free tropospheric ozone measurements. The Mie lidar and ozone DIAL were synchronized by two pulse-delay generators.

The 276/287 nm and 287/299 nm wavelength pairs were used for ozone DIAL measurements in the altitude ranges 0.57–2.0 km and 2.0–6.0 km, respectively. The effective vertical resolutions were 270 m for 0.57–2.0 km and 540 m for 2.0–6.0 km, respectively (Uchino et al., 2014). The time resolution was set to 1 h to facilitate comparison with the MRI-CCM2. An aerosol correction was not made for ozone retrieval. Next, we report the continuous lidar observational results made at Saga from 20 March to 31 March 2015.

3 Ozone DIAL data

Figure 2a shows a time-altitude cross-section of ozone volume mixing ratios observed by DIAL at Saga

151 from 11:10 JST on 20 March to 14:33 JST on 31 March 2015. Lidar observations were not obtained from
152 15:56 JST on 27 March to 21:58 JST on 29 March 2015, mainly because conditions were rainy or cloudy.
153 We made quality checks of the DIAL data. The gray regions in Fig. 2a correspond to areas where there
154 were no observational data or the errors were larger than 10%. The errors were computed from the lidar
155 signal-to-noise ratios by use of Poisson statistics. Regions surrounded by a black rectangle are areas
156 where the data were affected by aerosols and/or clouds with *R* larger than 2 at 299 nm. We calculated R
157 assuming *LR* = 50 sr, without correcting for attenuation by ozone absorption. In the lowest row of Fig. 2a,
158 we show hourly data of surface oxidant volume mixing ratios (Ox) at Takagimachi in Saga city measured
159 by the Saga Prefectural Environmental Research Center (https://www.pref.saga.lg.jp/web/at-
160 contents/kankyo1/shisetsu/_40810/_41304/_67819.html). Takagimachi is located about 2.8 km northeast
161 from the ozone DIAL site. Because the surface Ox was observed by a UV photometer, the contribution of
162 other components such as peroxyacetyle nitrate (PAN) to oxidant concentrations was extremely low, and
163 the oxidant volume-mixing ratio was considered to be that of ozone.
164 Figure 2a indicates that the ozone volume mixing ratios measured by DIAL were usually about 50–70
165 ppbv during the study period. Comparatively high ozone concentrations, >75 ppbv, were detected at
166 altitudes of 0.57–3 and 0.57–2 km on 20–23 March and 30–31 March, respectively. Notably high ozone
167 volume mixing ratios of 90–110 ppbv at altitudes of 0.57–1.5 km were observed from 03:00 to 20:00 JST
168 on 22 March. These high ozone concentrations were also seen in the surface photochemical oxidants data,
169 i.e., the Ox equaled 92–101 ppbv from 15:00 to 21:00 JST on 22 March, as shown in the lowest row in
170 Fig. 2a. The maximum concentration of Ox was 101 ppbv at 16:00 JST. This maximum value was far
171 above the environmental quality standard of 60 ppbv for hourly photochemical oxidants in Japan
172 (https://www.env.go.jp/en/air/aq/aq.html).
173
174 **3.1 Comparison of DIAL data with MRI CCM-2**
175
176 The MRI-CCM2 is a global model that simulates chemical and physical processes that affect the
177 distribution and evolution of ozone and other trace gases from the surface to the stratosphere (Deushi and
178 Shibata, 2011). Uchino et al. (2014) have provided an outline of MRI-CCM2. The vertical resolution of
179 the model increases from about 100 to 600 m from the surface to 6 km. The time step of the transport
180 (chemistry) scheme is 30 (15) min. We used hourly model output data. The horizontal resolution is about
181 110 km. We examined whether or not the model could simulate DIAL observational results. The MRI-
182 CCM2 simulated the DIAL observations reasonably well. However, the MRI-CCM2 predicted high ozone
183 concentrations of 50–60 ppbv and could not reproduce the concentrations of 90–110 ppbv observed with
184 DIAL below an altitude of 1.5 km during 03:00–20:00 JST on 22 March 2015.
185 We therefore performed some simulations in which we changed the emission inventory data and the
186 term that forced the reanalysis wind field. The most reasonable results, shown in Fig. 2b, were obtained
187 when the following changes were made. The e-folding time of the nudging term was changed from 18
188 hours to 12 hours to more strongly force the simulated wind fields toward the reanalysis data. In addition,

189 we changed the emission inventory of Regional Emission inventory in Asia version 1.1 (REAS 1.1)
190 (Ohara et al., 2007) to the REAS 2.1 emission inventory in 2007 (Kurokawa et al., 2013) and the
191 NO_2/NO_x emissions ratio from 5% to 15% by volume, which is within the range of uncertainty (Carslaw,
192 2005). The emission inventory of NO_x increased about 50% from REAS 1.1 to REAS 2.1. Figure 2c
193 shows the differences between the observed and simulated ozone mixing ratios. Simulated ozone volume
194 mixing ratios were about 60–70 ppbv below an altitude of 1.5 km from 14:00 JST on 21 March to 21:00
195 JST on 22 March 2015, lower by about 20–50 ppbv compared with the DIAL results. Moreover, the MRI-
196 CCM2 predicted high ozone concentrations a half-day earlier than the DIAL observations.
197 The maximum bias (systematic error) of ozone DIAL data caused by aerosols was estimated to be 20%
198 (15 ppbv) at 0.57 km; the mean bias and its standard deviation were 7 ± 5% in the altitude range 0.57–2.0
199 km at 11:00 JST. These biases were estimated from *Alp* observed at the same time by Mie lidar and
200 assuming LR = 50 sr in the wavelength range 276–299 nm based on equations (6) and (7) in Uchino and
201 Tabata (1991). These biases were not large because the 276/287 nm and 287/299 nm wavelength pairs are
202 suitable for measurements of ozone in the boundary layer and the free troposphere, respectively
203 (Nakazato et al., 2007). As mentioned earlier, ozone DIAL data with a statistical error smaller than 10%
204 were used in this study. Therefore, the uncertainty of the ozone DIAL data was estimated to be smaller
205 than 22%, and the mean value of the uncertainty was 12%. A model with higher horizontal resolution
206 might be necessary to more realistically simulate high surface ozone concentration events in the planetary
207 boundary layer.
208
209
210 **4 Mie lidar data**
211
212 Figures 3a, 3b, and 3c show time-altitude cross-sections of the backscattering ratio (R), the total volume
213 depolarization ratio (D), and the particle depolarization ratio (D_p), respectively, observed by Mie lidar at
214 Saga from 09:24 JST on 20 March to 14:34 JST on 31 March 2015. Mie lidar data were not obtained from
215 15:56 JST on 27 March to 21:58 JST on 29 March 2015, mainly because conditions were rainy or cloudy.
216 We made quality checks of Mie lidar data. Gray regions are areas where there were no observational data
217 or the data were affected by clouds.
218 Aerosol layers with R in the range 2–4 almost always existed below an altitude of 2.5 km during 20–
219 31 March 2015. An event of high aerosol loading with large values of R (>8) was observed below
220 altitudes of 1.5 km during 03:00–21:00 JST on 22 March, when the values of D were small (the mean ±
221 standard deviation was 3.9 ± 2.1%) compared with those before and after the event. The values of D were
222 larger than 7.9 ± 2.1% from 15:00 JST on 21 March through 15:00 JST on 23 March, except for 03:00–
223 21:00 JST on 22 March. The main aerosol component during the event might have been submicrometer-
224 sized spherical particles, because D_p was small (4 ± 2%), and the wavelength exponent *Alp* was large (1.3
225 ± 0.3). In contrast, the main aerosol particles before and after the event may have been supermicrometer-
226 sized, nonspherical mineral dust particles because D_p was comparatively large (13 ± 3%) and *Alp* was 1.0

± 0.2 (Sakai et al., 2003; Cattrall et al., 2005). When there were no clouds above, R at 1064 nm was estimated assuming Alp = 1.5 at the reference altitude, where very small amounts of aerosols were expected to be present, i.e., R = 1.06 ± 0.06 (D = 1.2 ± 0.5) at 532 nm in the altitude range 3–6 km. If the value of Alp was changed from 1.0 to 2.0 at the reference altitude, the uncertainty in Alp was estimated to be ± 0.2. Alp was 0.3–2.0 in the 11-day Mie lidar record. The maximum errors of D and D_p were 0.1% and 2% for R>2 at 532 nm.

During the same time period, high aerosol concentrations were also observed at the surface (Fig. 4). Hourly values of the mass concentrations of particulate matter with a diameter of 2.5 μm or less ($PM_{2.5}$) at Takagimachi measured by the Saga Prefectural Environmental Research Center were 23 μg m^{-3} at 10:00 JST and increased up to a maximum value of 110 μg m^{-3} at 15:00 JST on 22 March; the concentrations were greater than 82 μg m^{-3} during 13:00–16:00 JST and decreased to 17 μg m^{-3} at 01:00 JST on 23 March. The daily mean value of $PM_{2.5}$ was 50.6 μg m^{-3} for 24 hours on 22 March at Takagimachi, larger than the environmental quality standard of 35 μg m^{-3} in Japan (https://www.env.go.jp/en/air/aq/aq.html).

4.1 Comparison of Mie lidar data with MASINGAR mk-2

The MASINGAR-mk2 is an improved version of the MASINGAR aerosol model (Tanaka et al., 2003); it treats five aerosol species: sulfate, black and organic carbon, sea salt, and soil dust. We used emission data for sulfur dioxide and for black and organic carbon from MACCity (Granier et al., 2011). Soil dust and sea salt were represented by 10 bins with particle diameters of 0.2–20 μm. The model was coupled online with the atmospheric general circulation model MRI-AGCM3 (Yukimoto et al., 2012). The Meteorological fields were taken from JMA Global Analysis data (GANAL). The horizontal resolution of the MASINGAR-mk2 was about 60 km, and the number of vertical layers was 40 from the surface to 0.1 hPa. The vertical resolutions were 100, 300, and 600 m at the lowest level and altitudes of 1 and 6 km, respectively. The time step of the transport (chemistry) scheme was 450 seconds, and we used hourly model output data.

Figures 5a and 5b show the time-height cross sections of aerosol extinction coefficients observed by Mie lidar and simulated by MASINGAR-mk2, respectively. Figure 5c represents the difference between the observed and simulated extinction coefficients. The model was able to capture the general characteristics of the observational results rather well. A close look at Fig. 5c reveals that the model underestimated the aerosol extinction coefficients of the anthropogenic pollutant event on 22 March but slightly overestimated the extinction coefficients associated with particles having larger total volume depolarization ratios on 30 and 31 March (i.e., dust-dominant case).

4.2 Comparison of aerosol optical depths

Figure 6 shows temporal variations of the aerosol optical depths (AOD) measured by Mie lidar at 532 nm and sky radiometer at 500 nm (Kobayashi et al., 2006, Uchino et al., 2012a) and simulated at 550 nm by

MASINGAR-mk2 from 20 to 31 March. To estimate AODs from the lidar data, the extinction coefficient at 225 m was extrapolated to the ground, the extinction coefficient from 15 to 35 km was observed at night on the same day, and *S* was assumed to be 50 sr for all altitudes. When clouds and thick aerosols were present, AODs were not obtained. The sky radiometer was positioned on the roof of the building, which is four stories high and located to the west of the container (brown building in Fig. 1). Although it must be noted that the measured and simulated wavelengths differed slightly, the AODs were almost the same, except for the high aerosol and ozone event on 22 March. The mean bias ± the standard deviation of the AOD between Mie lidar and sky radiometer was 0.029 ± 0.051, and that between MASINGAR mk-2 and sky radiometer was –0.07 ± 0.24 for 20–31 March, except for 12:00–14:00 JST on 22 March. The maximum values of the AODs were 2.1 at 12:00 JST by lidar, 1.92 at 13:00 JST by sky radiometer, and 0.53 at 13:00 JST by MASINGAR-mk2. One possible reason for the large difference in AOD (~0.2) between Mie lidar and Sky radiometer data is that we set the reference altitudes to 8.2 km and 2.8 km at 12:00 and 13:00 JST on 22 March, respectively, for the lidar because the backscattered signals were strongly attenuated by the dense aerosol layers below 2 km. This might have caused errors in the AODs for the Mie lidar data. The possibility that the views obtained by the sky radiometer and Mie lidar differed might also account for the difference.

The model underestimated the AODs by factors of about 3.6–4 compared to the sky radiometer and lidar observations. One plausible reason for that is that the model resolution (about 60 km) was insufficient to reproduce the observed prominent peak in which the observed AOD increased from 1.0 to 2.0 in 6 hours. The other plausible reason for the underestimation is the uncertainty of the emissions inventories of aerosol precursors. Grainer et al. (2011) collected various emission inventories and compared them on a global scale. They found that differences in Chinese sulfur dioxide (SO_2) emissions in 2000 reached 66% between the lowest and highest emissions and concluded that there was no consensus among the different inventories for the emissions of Chinese SO_2. This large variation among the inventories indicates that there is a large error associated with the estimate of SO_2 emission in China. In their comparison, the MACCity emission, which was used in the MASINGAR-mk2 simulation, showed the lowest amount of Chinese SO_2 emission among the inventories. This might explain the underestimation of pollutant aerosol (sulfate) concentrations. In the MASINGAR-mk2 simulation, the dust emission flux was estimated by a parameterized dust emission scheme and was strongly dependent on various parameters (e.g., soil texture, soil wetness, land use, snow cover fraction, vegetation cover, and surface wind speed). The dust model intercomparison project (DMIP; Uno et al., 2006) reported that simulated amounts of dust emissions over East Asia differed sometimes by a factor of ten among eight dust models (including the former version of MASINGAR). These facts indicate that estimates of dust emissions are associated with large errors. To solve this problem, for example, it might be better to use the near real-time satellite data of SO_2 and nitrogen dioxide (NO_2) provided by the Ozone Monitoring Instrument (OMI) onboard NASA's Aura satellite (Krotkov et al., 2016), and/or to use a data assimilation technique that integrates model simulation and observational data (Yumimoto et al., 2016).

5 Discussion: origin and transport pathways of ozone and aerosol plumes

Figure 7 shows the time-altitude cross sections of total aerosol extinction coefficients at 550 nm, and the ratios of dust extinction coefficients to total aerosol extinction coefficients simulated by MASINGAR-mk2 with potential temperatures over Saga for 20–31 March 2015. For the event on 22 March, the model predicted dust particles (about 60–100%) in the altitude range 1–3 km, and it predicted sulfate (about 40–60%) and dust (about 30–40%) particles below 1 km. The numbers in parentheses indicate the ratio of each component's extinction coefficient to the total extinction coefficient. The dust particles descended to the surface in the afternoon (Fig.7b). For the event on 30 March, MASINGAR mk-2 predicted dust particles (about 50–100%) at altitudes of 1–6 km, and it predicted sulfate (about 50–80%) and dust (about 0–20%) particles below 1 km in the morning. Mie lidar data supported the model prediction because D_p was high (17 ± 6%) at altitudes of 1–3 km and low (10 ± 3%) below 1 km. For both events, small amounts of organic carbon, black carbon, and sea salt particles were predicted.

To identify the origin of the aerosols and related transport processes, three-dimensional backward trajectories of air parcels were calculated with the NOAA Hybrid Single Particle Lagrangian Integrated Trajectory (HYSPRIT) model (Draxler and Hess, 1998; Stein et al., 2015). Air parcels were initially left at altitudes of 1500 m (Fig. 8a) and 500 m (Fig. 9a) over the lidar site at Saga. The trajectories were calculated for three days from 21:00 UTC on 21 (06:00 JST on 22) March 2015. Figures 8b and 9b show the time-altitude cross sections of dust and sulfate extinction coefficients simulated by MASINGAR mk-2 along the trajectory paths of Figs. 8a and 9a, respectively. Based on the results of the backward trajectories and the model simulations, the dust and sulfate particles on 22 March could have been transported within about two days from the Gobi Desert and the North China Plain (NCP), respectively, to the measurement site. The MASINGAR mk-2 simulation suggested that the dust particles emitted during 18:00–24:00 UTC on 19 March around 40°N and 105°E were responsible for the dust storm captured by the Mie lidar observation. The highest concentrations of SO_2 and NO_2 in the world were observed in the NCP during 2013–2015 by the Ozone Monitoring Instrument (OMI) onboard NASA's Aura satellite, as shown in Fig. 5 by Krotkov et al. (2016). These gases are important precursors of sulfate particles and ozone. Figure 10 shows horizontal maps of ozone volume mixing ratios at 925 hPa (an altitude of about 760 m) simulated by the MRI-CCM2 at 21:00 JST on 19, 20, and 21 March and at 03:00 JST on 22 March 2015. These maps indicate that the high ozone concentrations could have been transported from the NCP to the Yellow Sea and then to Saga within about two days.

Because it was difficult to obtain observational data of surface ozone and sulfate particles over the NCP, including Beijing, on 19–20 March, we referred to the following papers with respect to those data. According to the ozonesonde measurements made by Wang et al. (2012), ozone concentrations ≥90 ppbv were observed over Beijing, China in late March. Ma et al. (2016) reported a significant increase of surface ozone from 2003 to 2015 at Shangdianzi (40.65°N, 117.10°E), which is located about 100 km northeast of suburban Beijing, and the maximum daily average 8-h concentrations of ozone appear to

have been >100 ppbv in March 2015 based on Fig. 2 in their paper. High $PM_{2.5}$ and submicron aerosol concentrations have been observed in Beijing (Zhang et al., 2013; Sun et al., 2015). Ozone and aerosol concentrations may therefore have been high in March 2015 over the NCP.

To elucidate the vertical transport processes of the aerosol and ozone in the lower troposphere over the measurement site, we show in Fig. 11 the time variations of the heights of the mixed layers from two hours after sunrise to two hours before sunset during 09:24 JST on 20 March through 14:34 JST on 31 March 2015. These altitudes were estimated from (1) the 1064 nm range-corrected backscatter signals, with a range resolution of 15 m and a time interval of 20 min, using the wavelet covariance transform method (Baars et al., 2008; Izumi et al., 2016) and (2) signals obtained from radiosonde data at Fukuoka and the JMA Meso-scale Analysis (MA) data over Saga using the parcel method (Holzworth, 1964). When the mixed layers developed in the afternoon, the heights of the mixed layers (1.5–2 km) estimated by Mie lidar were similar to those estimated by MA. Although the radiosonde data at 9:00 JST on 22 March found the height of the mixed layer to be 117 m (Stull, 1988), it was difficult for Mie lidar to detect the mixed layer because the lowest altitude of the Mie lidar measurement was 225 m.

The dust particles that originated from the Gobi Desert arrived at altitudes of 1–3 km over the lidar site at 06:00 JST on 22 March. When the mixed layer developed to 1.5–2 km at 11:00–15:00 JST on 22, the dust particles were assumed to be mixed into the boundary layer and then to reach the surface by entrainment, as simulated in Fig. 7b. This may explain the sharp increase in PM2.5 concentrations at the surface after 11:00 JST, as shown in Fig. 4. A similar phenomenon was observed over the northern Kyushu area during the dust event in late May–early June 2014 (Uno et al., 2016). A similar high-surface-ozone event was observed by eight ozonesonde measurements during 6–9 June 2003 over the Seoul metropolitan region (Oh et al., 2010).

6. Concluding remarks

By using ozone DIAL and a two-wavelength polarization (Mie) lidar, we made continuous measurements of ozone and aerosol concentrations over Saga during 20–31 March 2015. High ozone and high aerosol concentrations that occurred nearly simultaneously were observed in the altitude range 0.5–1.5 km from 03:00 to 20:00 JST on 22 March 2015. The ozone volume mixing ratio was larger than 100 ppbv. The aerosol extinction coefficient and AOD at 532 nm were larger than 0.5 km^{-1} and 1.5, respectively.

Backward trajectory analysis and the simulations by the MASINGAR mk-2 and the MRI-CCM2 models indicated that mineral dust particles from the Gobi Desert and an air mass with high ozone and aerosol (mainly sulfate) concentrations that originated from the North China Plain could have been transported over the lidar site within about two days. Based on the lidar and surface measurement data and the simulation by the MASINGAR-mk2, there is a possibility that the air mass with high ozone and aerosol concentrations could have been transported from the lower troposphere to the surface by vertical mixing when the planetary boundary layer developed in the afternoon of 22 March 2015. The

379 combination of ozone DIAL measurements with surface in-situ ozone measurements is very useful for
380 studying the process of descent of high ozone concentrations in the lower troposphere to the surface and
381 the impacts on surface air quality. Such measurements of pollution plumes that descend from the free
382 troposphere to the surface are highly recommended (HTAP, 2010).
383 The MRI-CCM2 could approximately reproduce the high-ozone volume-mixing ratios after some
384 modifications of physical and chemical parameters. MASINGAR mk-2 successfully predicted high
385 aerosol concentration events, but the predicted peak AOD was about one-third of the observed AOD. For
386 further improvement of these models, it will be important to continue comparing these models with ozone
387 DIAL, Mie lidar, and surface in-situ ozone and particle measurements.
388
389 *Acknowledgements.* We used radiosonde data measured by the Japan Meteorological Agency and hourly
390 concentrations of surface oxidant and $PM_{2.5}$ measured by the Saga Prefectural Environmental Research
391 Center. The NOAA Hybrid Single Particle Lagrangian Integrated Trajectory (HYSPRIT) model was used
392 to calculate backward trajectories of air parcels. The authors thank the anonymous referees and editors for
393 helpful comments and suggestions.
394
395
396
397
398
399
400
401
402
403
404
405
406
407
408
409
410
411
412
413
414
415
416

417 **References**

418 Akimoto, H., Mukai, H., Nishikawa, M., Murano, K., Hatakeyama, S., Liu, C., Buhr, M., Hsu, K. J.,
419 Jaffe, D. A., Zhang, L., Honrath, R., Merrill, J. T., and Newell, R. E.: Long-range transport of ozone in
420 the East Asian Pacific rim region, J. Geophys. Res., 101, D1, 1999-2010, 1996.
421 Ancellet, G. and Ravetta, F.: Analysis and validation of ozone variability observed by lidar during the
422 ESCOMPTE-2001 campaign, Atmos. Res., 74, 435-459, 2005.
423 Anderson, T. L., Masonis, S. J., Covert, D. S., Ahlquist, N. C., Howell, S. G., Clarke, A. D., and
424 McNaughton, C. S.: Variability of aerosol optical properties derived from in situ aircraft
425 measurements during ACE-Asia, J. Geophys. Res., 108, D23, 8647, doi:10.1029/2002JD003247, 2003.
426 Baars, H., Ansmann, A., Engelmann, R., and Althausen, D.: Continuous monitoring of the boundary-layer
427 top with lidar, Atmos. Chem. Phys., 8, 7281-7296, 2008.
428 Bak, J., Kim, J. H., Liu, X., Chance, K., and Kim, J.: Evaluation of ozone profile and tropospheric ozone
429 retrievals from GEMS and OMI spectra, Atmos. Meas. Tech., 6, 239-249, doi:10.5194/amt-6-239-
430 2013, 2013.
431 Banta, R. M., Senff, C. J., White, A. B., Trainer, M., McNider, R. T., Valente, R. J., Mayor, S. D., Alvarez,
432 R. J., Hardesty, R. M., Parrish, D., and Fesenfeld, F. C.: Daytime buildup and nighttime transport of
433 urban ozone in the boundary layer during a stagnation episode, J. Geophys. Res., 103, D17, 22519-
434 22544, 1998.
435 Carslaw, D. C.: Evidence of an increasing NO_2/NO_x emissions ratio from road traffic emissions, Atmos.
436 Env., 39, 4793-4802, 2005.
437 Cattrall, C., Reagan, J., Thome, K., and Dubovik, O.: Variability of aerosol and spectral lidar and
438 backscatter and extinction ratios of key aerosol types derived from selected Aerosol Robotic Network
439 locations, J. Geophys. Res., 110, D10S11, doi:10.1029/2004JD005124, 2005.
440 Deushi, M. and Shibata, K.: Development of a Meteorological Research Institute Chemistry-Climate
441 Model version 2 for the study of tropospheric and stratospheric chemistry, Pap. Meteorol. Geophys.,
442 62, 1-46, doi:10.2467/mripapers.62.1, 2011.
443 Draxler, R. R. and Hess, G. D.: An overview of the HYSPLIT_4 modeling system for trajectories,
444 dispersion, and deposition, Aust. Meteor. Mag., 47, 295-308, 1998.
445 Eisele, H. and Trickl, T.: Improvements of the aerosol algorithm in ozone lidar data processing by use of
446 evolutionary strategies, 44, 2638-2651, 2005.
447 Fernald, F. G.: Analysis of atmospheric lidar observations: some comments, Appl. Opt., 23, 652-653,
448 1984.
449 Granier, C., Bessagnet, B., Bond, T., D'Angiola, A., van der Gon, H. D.., Frost, G. J., Heil, A., Kaiser, J.
450 W., Kinne, S., Klimont, Z., Kloster, S., Lamarque, J. -F., Liousse, C., Masui, T., Meleux, F., Mieville,
451 A., Ohara, T., Raut, J.-C., Riahi, K., Schultz, M. G., Smith, S. J., Thompson, A., van Aardenne, J., van
452 der Werf, G. R., and van Vuuren, D. P.: Evolution of anthropogenic and biomass burning emission of
453 air pollutants at global and regional scales during the 1980–2010 period, Clim. Change, 109, 163–190,
454 2011.

455 Hara, Y., Yumimoto, K., Uno, I., Shimizu, A., Sugimoto, N., Liu, Z., and Winker, D. M.: Asian dust
456 outflow in the PBL and free atmosphere retrieved by NASA CALIPSO and an assimilated dust
457 transport model, Atmos. Chem. Phys., 9, 1227-1239, 2009.
458 Hemispheric Transport of Air Pollution (HTAP) 2010, Part A: Ozone and particulate matter, edited by:
459 Dentener, F., Keating, T., and Akimoto, H., Air Pollution Studies No. 17, United Nations, New York
460 and Geneva, 278 pp., 2010.
461 Holzworth, G. C.: Estimates of mean maximum mixing depths in the contiguous United States, Mon.
462 Weather Rev., 92, 235-242, 1964.
463 Houweling, S., Hartmann, W., Aben, I., Schrijver, H., Skidmore, J., Roelofs, G.-J., and Breon, F.-M.:
464 Evidence of systematic errors in SCIAMACHY-observed CO_2 due to aerosols, Atmos. Chem. Phys., 5,
465 3003-3013, 2005.
466 Intergovernmental Panel on Climate Change (IPCC): Climate Change 2013: The Physical Science Basis:
467 Contribution of Working Group I to the Fifth Assessment Report of the Intergovernmental Panel on
468 Climate Change, edited by: Stocker, T.F., Qin, D., Plattner, G.-K., Tignor, M., Allen, S.K., Boschung,
469 J., Nauels, A., Xia, Y., Bex, V., and Midgley, P.M., Cambridge University Press, Cambridge, United
470 Kingdom and New York, NY, USA, 1535 pp, doi:10.1017/CBO9781107415324, 2013.
471 Iwasaka, Y., Yamato, M., Imasu, R., and Ono, A.: Transport of Asian dust (KOSA) particles; importance
472 of weak KOSA events on the geochemical cycle of soil particles, Tellus, 40B, 494-503, 1988:
473 Izumi, T., Uchino, O., Sakai, T., Nagai, T., and Morino, I.: Mixed layer height calculated from Mie lidar
474 data, submitted to Tenki, 2016 (in Japanese).
475 Kobayashi, E., Uchiyama, A., Yamazaki, A., and Matsuse, K: Application of the maximum likelihood
476 method to the inversion algorithm for analyzing aerosol optical properties from sun and sky radiance
477 measurements, J. Meteor. Soc. Jpn., 84, 1047-1062, 2006.
478 Kourtidis, K., Zerefos, C., Rapsomanikis, S., Simeonov, V., Balis, D., Perros, P. E., Thompson, A. M.,
479 Witte, J., Calpini, B., Sharobiem, W. M., Papayannis, A., Mihalopoulos, N., and Drakou, R.: Regional
480 levels of ozone in the troposphere over eastern Mediterranean, J. Geophys. Res., 107, D18, 8140,
481 doi:10.1029/2000JD000140, 2002.
482 Krotkov, N. A., McLinden, C. A., Li, C., Lamsal, L. N., Celarier, E. A., Marchenko, S. V., Swartz, W. H.,
483 Bucsela, E. J., Joiner, J., Duncan, B. N., Boersma, K. F., Veefkind, J. P., Levelt, P. F., Fioletov, V. E.,
484 Dickerson, R. R., He, H., Lu, Z., and Streets, D. G.: Aura OMI observations of regional SO_2 and NO_2
485 pollution changes from 2005 to 2015, Atmos. Chem. Phys., 16, 4605-4629, doi:10.5194/acp-16-4605-
486 2016, 2016.
487 Kuang, S., Newchurch, M. J., Burris, J., Wang, L., Buckley, P. I., Johnson, S., Knupp, K., Huang, G.,
488 Phillips, D., and Cantrell, W.: Nocturnal ozone enhancement in the lower troposphere observed lidar,
489 Atmos. Environ., 45, 6078-6084, 2011.
490 Kurokawa, J., Ohara, T., Morikawa, T., Hanayama, S., Janssens-Maenhout, G., Fukui, T., Kawashima,
491 K., and Akimoto, H.: Emissions of air pollutants and greenhouse gases over Asian regions during
492 2000–2008: Regional Emission inventory in ASia (REAS) version 2, Atmos. Chem. Phys., 13, 11019–

493 11058, doi: 10.5194/acp-13-11019-2013, 2013.
494 Ma, Z., Xu, J., Quan, W., Zhang, Z., Lin, W., and Xu, X.: Significant increase of surface ozone at a rual
495 site, north of eastern China, Atmos. Chem. Phys., 16, 3969-3977, doi:10.5194/acp-16-3969-2016,
496 2016.
497 Murayama, T., Sugimoto, N., Uno, I., Kinoshita, K., Aoki, K., Hagiwara. N., Liu, Z., Matsui, I., Sakai, T.,
498 Shibata, T., Arao, K., Sohn, B. J., Won, J. G., Yoon, S. C., Li, T., Zhou, J., Hu, H., Abo, M., Iokibe,
499 K., Koga, R., and Iwasaka, Y.: Ground-based network observation of Asian dust events of April 1998
500 in east Asia, J. Geophys. Res., 106, D16, 18345-18359, 2001.
501 Nakazato, M., Nagai, T., Sakai, T., and Hirose, Y.: Tropospheric ozone differential-absorption lidar using
502 stimulated Raman scattering in carbon dioxide, Apl. Opt., 46, 2269-2279, 2007.
503 Oh, I.-B., Kim, Y.-K., Hwang, M.-K., Kim, C.-H., Kim, S., and Song, S.-K.: Elevated ozone layers over
504 the Seoul metropolitan region in Korea: evidence for long-range ozone transport from eastern China
505 and its contribution to surface concentrations, J. Appl. Meteor. and Climat., 49, 203-220,
506 doi:10.1175/2009JAMC2213.1, 2010.
507 Ohara, T., Akimoto, H., Kurokawa, J., Horii, N., Yamaji, K., Yan, X., and Hayasaka, T.: An Asian
508 emission inventory of anthropogenic emission sources for the period 1980-2020, Atmos. Chem. Phys.,
509 7, 4419-4444, doi:10.5194/acp-7-4419-2007, 2007.
510 Ohyama, H., Kawakami, S., Shiomi, K., and Miyagawa, K.: Retrievals of total and tropospheric ozone
511 from GOSAT thermal infrared spectral radiances, IEEE Trans. Geosci. Remote Sens., 50, 1770-1784,
512 doi:10.1109/TGRS.2001.2170178, 2012.
513 Sakai, T., Nagai, T., Nakazato, M., Mano, Y., and Matsumura, T.: Ice clouds and Asian dust studied with
514 lidar measurements of particle extinction-to-backscatter ratio, particle depolarization, and water-vapor
515 mixing ratio over Tsukuba, Appl. Opt., 42, 7103-7116, 2003.
516 Stein, A. F., Draxler, R. R., Rolph, G. D., Stunder, B. J. B., Cohen, M. D., and Ngan, F.: NOAA's
517 HYSPLIT atmospheric transport and dispersion modeling system, Bull. Amer. Meteor. Soc., 96, 2059-
518 2077, 2015.
519 Stull, R. B.: An introduction to boundary layer meteorology, Klumer Academic Publications, 670 pp,
520 1988.
521 Sun, Y. L., Wang, Z. F., Du, W., Zhang, Q., Wang, Q. Q., Fu, P. Q., Pan, X. L., Li, J., Jayne, J., and
522 Worsnop, D. R.: Long-term real-time measurements of aerosol particle composition in Beijing, China:
523 seasonal variations, meteorological effects, and source analysis, Atmos. Chem. Phys., 15, 10149-
524 10165, doi:10.5194/acp-15-10149-2015, 2015.
525 Tanaka, T. Y., Orito, K., T. T. Sekiyama, Shibata, K., Chiba, M., and Tanaka, H.: MASINGAR, a global
526 tropospheric aerosol chemical transport model coupled with MRI/JMA98 GCM: Model description,
527 Pap. Meteor. Geophys., 53(4), 119-138, 2003.
528 Uchino, O. and Tabata, I.: Mobile lidar for simultaneous measurements of ozone, aerosols, and
529 temperature in the stratosphere, Appl. Opt., 30, 2005-2012, 1991.
530 Uchino, O., Kikuchi, N., Sakai, T., Morino, I., Yoshida Y., Nagai, T., Shimizu, A., Shibata, T.,

Yamazaki, A., Uchiyama, A., Kikuchi, N., Oshchepkov, S., Brill, A., and Yokota, T., Influence of aerosols and thin cirrus clouds on the GOSAT-observed CO_2: a case study over Tsukuba, Atmos. Chem. Phys., 12, 3393–3404, doi:10.5194/acp-12-3393-2012, 2012a.

Uchino, O., Sakai, T., Nagai, T., Nakamae, K., Morino, I., Arai, K., Okumura, H., Takubo, S., Kawasaki, T., Mano, Y., Matsunaga, T., and Yokota, T., On recent (2008–2012) stratospheric aerosols observed by lidar over Japan, Atmos. Chem. Phys., 12, 11975–11984, doi:10.5194/acp-12-11975-2012, 2012b.

Uchino, O., Sakai, T., Nagai, T., Morino, I., Maki, T., Deushi, M., Shibata, K., Kajino, M., Kawasaki, T., Akaho, T., Takubo, S., Okumura, H., Arai, K., Nakazato, M., Matsunaga, T., Yokota, T., Kawakami, S., Kita, K., and Sasano, Y.: DIAL measurement of lower tropospheric ozone over Saga (33.24°N, 130.29°E) , Japan, and comparison with a chemistry–climate model, Atmos. Meas. Tech., 7, 1385-1394, doi:10.5194/amt-7-1385-2014, 2014.

Uno, I., Wang, Z., Chiba, M., Chun, Y. S., Gong, S. L., Hara, Y., Jung, E., Lee, S.-S., Liu, M., Mikami, M., Music, S., Nickovic, S., Satake, S., Shao, Y., Song, Z., Sugimoto, N., Tanaka, T., and Westphal, D. L.: Dust model intercomparison (DMIP) study over Asia: Overview, J. Geophys. Res., 111, D12213, doi:10.1029/2005JD006575, 2006.

Uno, I., Pan, X., Itahashi, S., Yumimoto, K., Hara, Y., Kuribayashi, M., Yamamoto, S., Shimohara, T., Tamura, K., Ogata, Y., Osada, K., Kamikuchi, Y., Yamada, S., and Kobayashi, H.: Overview of long-range yellow sand and high concentration of air pollution observed over the northern Kyusyu area in late May-early June 2014, J. Jpn. Soc. Atmos. Environ., 51, 44-57, 2016.

Veefkind, J. P., Aben, I., McMullan, K., Förster, H., de Vries, J., Otter, G., Claas, J., Eskes, H. J., de Haan, J. F., Kleipool, Q., van Weele, M., Hasekamp, O., Hoogeveen, R., Landgraf, J., Snel, R., Tol, P., Ingmann, P., Voors, R., Kruizinga, B., Vink, R., Visser, H., and Levelt, P. F.: TROPOMI on the ESA Sentinel-5 Precursor: A GMES mission for global observations of the atmospheric composition for climate, air quality and ozone layer applications, Remote Sens. Environ., 120, 70-83, 2012.

Wang, Y., Konopka, P., Liu, Y., Che, H., Müller, R., Plöger, F., Riese, M., Cai, Z., and Lü, D.: Tropospheric ozone trend over Beijing from 2002-2010: ozonesonde measurements and modeling analysis, Atmos. Chem. Phys., 12, 8389-8399, doi:10.5194/acp-12-8389-2012, 2012.

Yamaji, K., T. Ohara, T., Uno, I., Tanimoto, H., Kurokawa, J., and Akimoto, H.: Analysis of the seasonal variation of ozone in the boundary layer in East Asia using the Community Multi-scale Air Quality model: What controls surface ozone levels over Japan? Atmos. Environ., 40, 1856-1868, 2006.

Yue, X. and Unger, N., Ozone vegetation damage effects on gross primary productivity in the United States, Atmos. Chem. Phys., 14, 9137-9153, doi:10.5194/acp-14-9137-2014, 2014.

Yukimoto, S., Adachi, Y., Hosaka, M., Sakami, T., Yoshimura, H., Hirabara, M., Tanaka, T. Y., Shindo, E., Tsujino, H., Deushi, M., Mizuta, R., Yabu, S., Obata, A., Nakano, H., Koshiro, T., Ose, T., and Kitoh, A.: A new global climate model of the Meteorological Research Institute: MRI-CGCM3 ―Model Description and Basic Performance―, J. Meterol. Soc. Jpn., 90A, 23-64, doi:10.2151/jmsj.2012-A02. 2012.

Yumimoto, K., Nagao, T. M., Kikuchi, M., Sekiyama, T. T., Murakami, H., Tanaka, T. Y., Ogi, A., Irie, H.,

569 Khatari, P., Okumura, H., Arai, K., Morino, I., Uchino, O., and Maki, T.: Aerosol data assimilation
570 using data from Himawari-8, a next-generation geostationary meteorological satellite, Geophys. Res.
571 Lett., 43, doi:10.1002/2016GL069298, 2016.
572 Zhang, R., Jing, J., Tao, J., Hsu, S.-C., Wang, G., Cao, J., Lee, C. S. L., Zhu, L., Chen, Z., Zhao, Y., and
573 Shen, Z.: Chemical characterization and source apportionment of $PM_{2.5}$ in Beijing: seasonal
574 perspective, Atmos. Chem. Phys., 13, 7053-7074, doi:10.5194/acp-13-7053-2013, 2013.
575
576
577
578
579
580
581
582
583
584
585
586
587
588
589
590
591
592
593
594
595
596
597
598
599
600
601
602
603
604
605
606

Table 1. Characteristics of Mie lidar

Transmitter			
Laser		Nd:YAG	
Wavelength	532 nm		1064 nm
Pulse energy	130 mJ		130 mJ
Pulse repetition rate		10 Hz	
Pulse width		8 ns	
Beam divergence	0.2 mrad		0.2 mrad
Receiver			
Telescope type		Schmidt Cassegrain	
Telescope diameter		30.5 cm	
Focal length		3048 mm	
Field of view		1 mrad	
Polarization	P and S		None
Number of channels	3		1
Interference filter			
Center wavelength	532.0 nm		1064.1 nm
Bandwidth (FWHM)	0.29 nm		0.38 nm
Transmission	0.66		0 .58
Detectors	PMT		APD
	(Hamamatsu R3234-01)		(EG&G C30956EH)
Signal processing	12bit A/D + Photon counting		
Time resolution	1 min		
Vertical resolution	7.5 m		

Table 2. Characteristics of tropospheric ozone DIAL system

Transmitter					
Pump laser	Nd:YAG				
Wavelength	266 nm				
Pulse energy	107 mJ				
Pulse repetition rate	10 Hz				
Pulse width	8 ns				
Raman active gas	CO_2				
Stokes lines	276 nm	287 nm	299 nm	312 nm	
Pulse energy	7.5 mJ	9.1 mJ	8.4 mJ	No. meas.	
Beam divergence	0.1 mrad				
Receiver					
Telescope type	Newtonian			Prime focus (fiber coupled)	
Telescope diameter	49 cm			10 cm	
Focal length	1750 mm			320 mm	
Field of view	1 mrad			3 mrad	
Interference filter					
Center wavelength	287.2 nm	299.0 nm	312.0 nm	276.1 nm	287.2 nm
Bandwidth (FWHM)	1.02 nm	1.15 nm	0.82 nm	1.07 nm	1.05 nm
Transmission	0.18	0.32	0.36	0.17	0.21
Detectors	PMT (Hamamatsu R3235-01)				
Signal processing	12bit A/D + Photon counting				
Time resolution	1 min				
Vertical resolution	7.5 m				

Figure 1. Mie lidar and ozone DIAL (right) were installed in the container at the left on the ground (left).

(a)

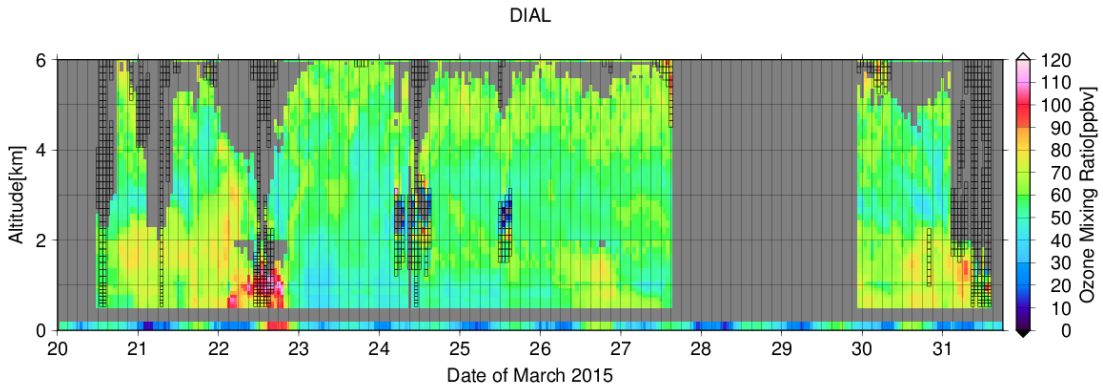

(b)

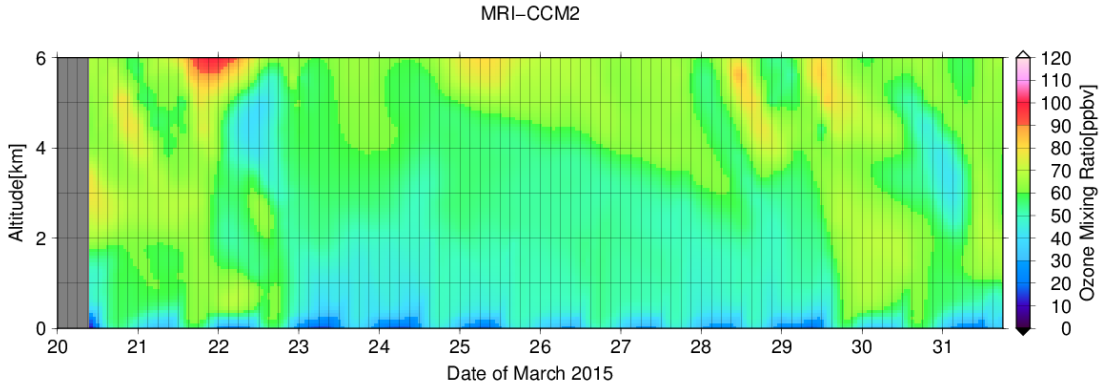

(c)

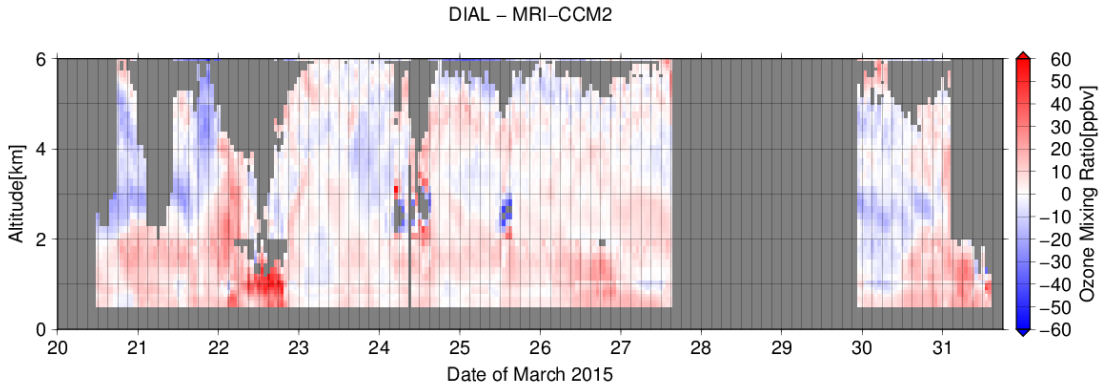

Figure 2. Time-altitude cross-sections of (a) ozone volume mixing ratios observed by DIAL over Saga from 11:10 JST on 20 March to 14:33 JST on 31 March 2015, (b) the ratios simulated by a modified MRI-CCM2 for 20–31 March 2015, and (c) the difference between the observed and simulated ozone volume mixing ratios (a–b). Gray regions indicate areas where there were no observational data or the statistical errors were larger than 10%. Regions enclosed with black rectangles are areas where the data were affected by aerosols and/or clouds. The lowest row in Fig. 2a shows photochemical oxidant (ozone) volume mixing ratios at Takagimachi in Saga city as measured by the Saga Prefectural Environmental Research Center.

(a)

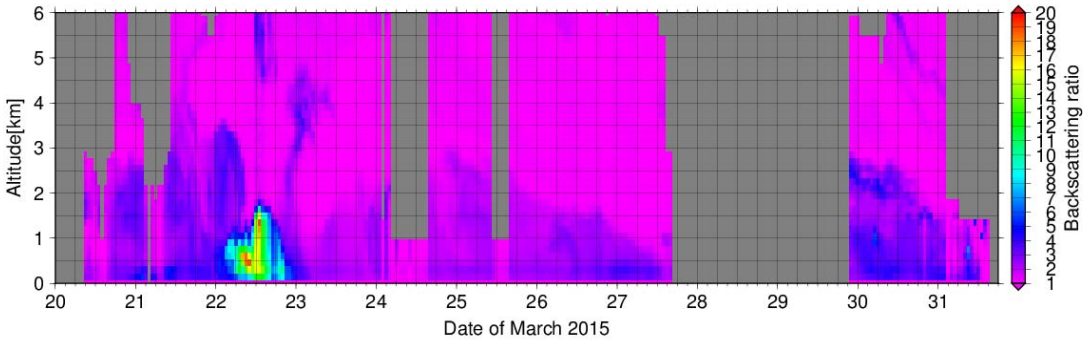

(b)

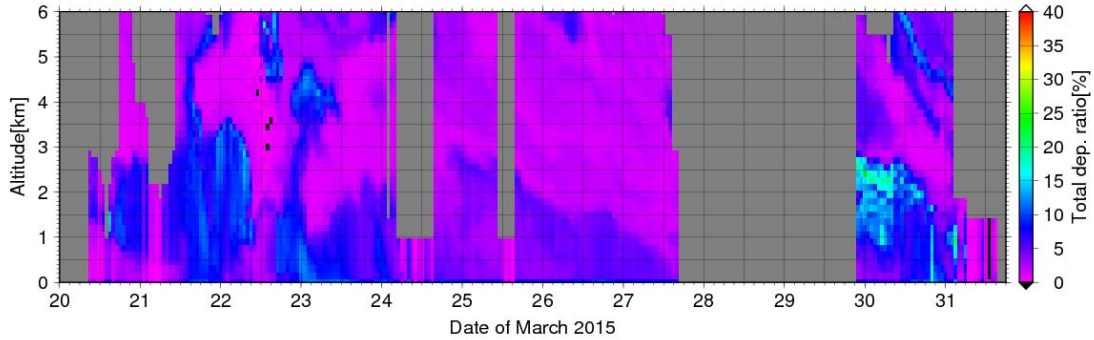

(c)

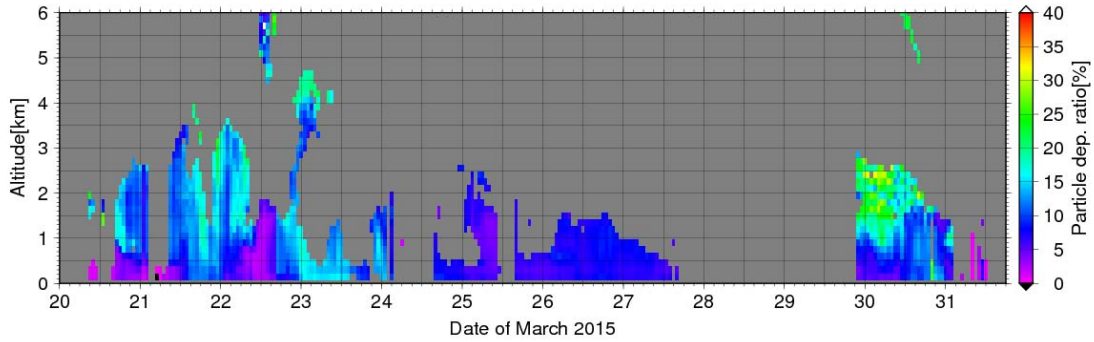

Figure 3. Time-altitude cross-sections of (a) backscattering ratios, (b) total volume depolarization ratios and, (c) particle depolarization ratios for $R \geq 2.0$ at 532 nm observed by Mie lidar at Saga from 09:24 JST on 20 March to 14:34 JST on 31 March 2015. Lidar observations were not available from 15:56 JST on 27 March to 21:58 JST on 29 March 2015 mainly because of rainy or cloudy conditions. Gray regions are areas where there were no observational data or where the observations were affected by clouds.

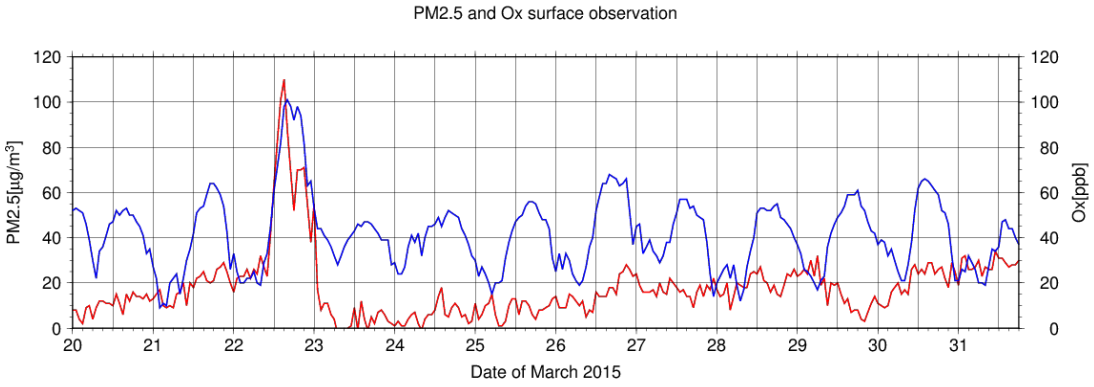

Figure 4. Hourly (JST) data of surface PM2.5 (red line) and Ox (blue line) measured by the Saga Prefectural Environmental Research Center for 20–31 March 2015. The volume mixing ratio of Ox was considered to be that of ozone.

(a)

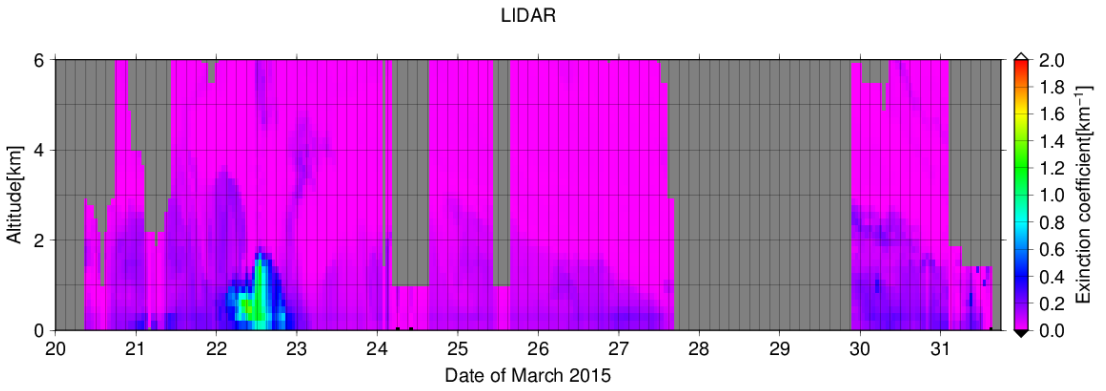

(b)

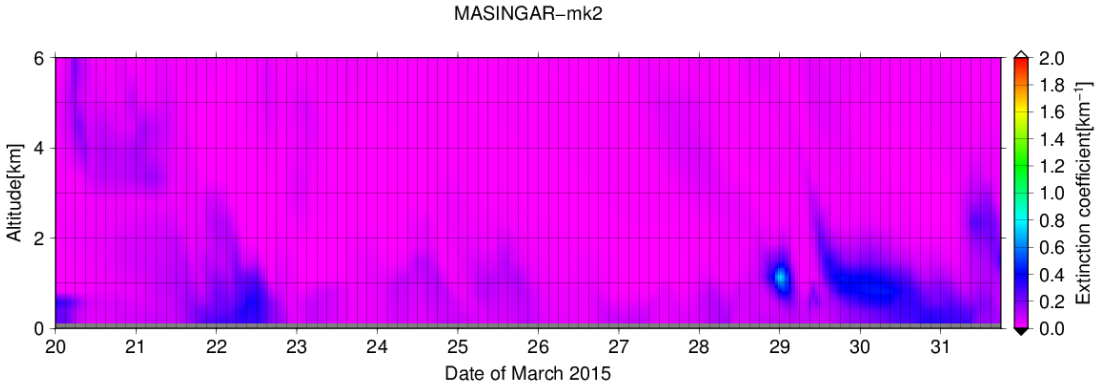

(c)

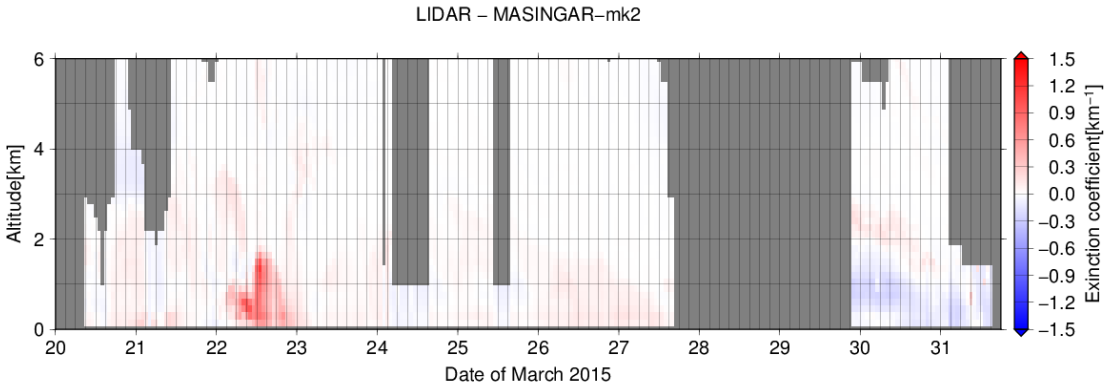

Figure 5. Time-altitude cross sections of (a) aerosol extinction coefficients observed by Mie lidar at 532 nm over Saga from 09:24 JST on 20 March to 14:34 JST on 31 March 2015, (b) the coefficients simulated by MASINGAR-mk2 at 550 nm for 20–31 March 2015, and (c) the difference between the Mie lidar observations and the simulation (a–b). Gray regions represent areas where there were no observational data.

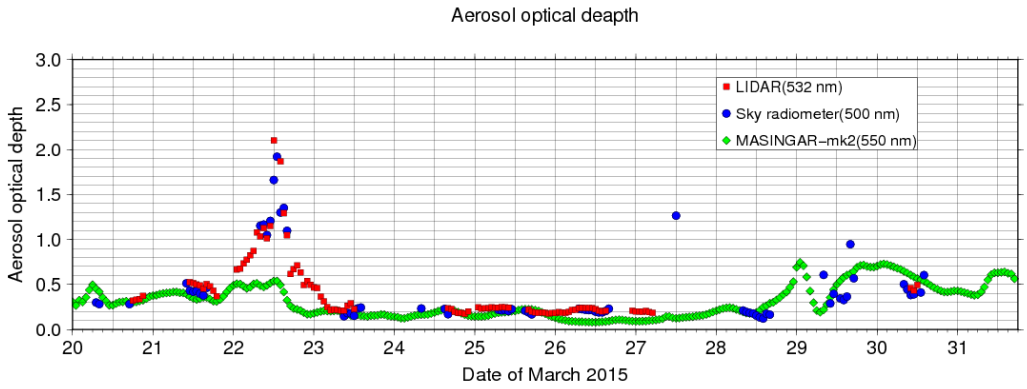

Figure 6. Temporal variation of the aerosol optical depth (AOD) measured by Mie lidar at 532 nm (red circles), by sky radiometer at 500 nm (blues circles), and simulated at 550 nm by MASINGAR-mk2 (green circles).

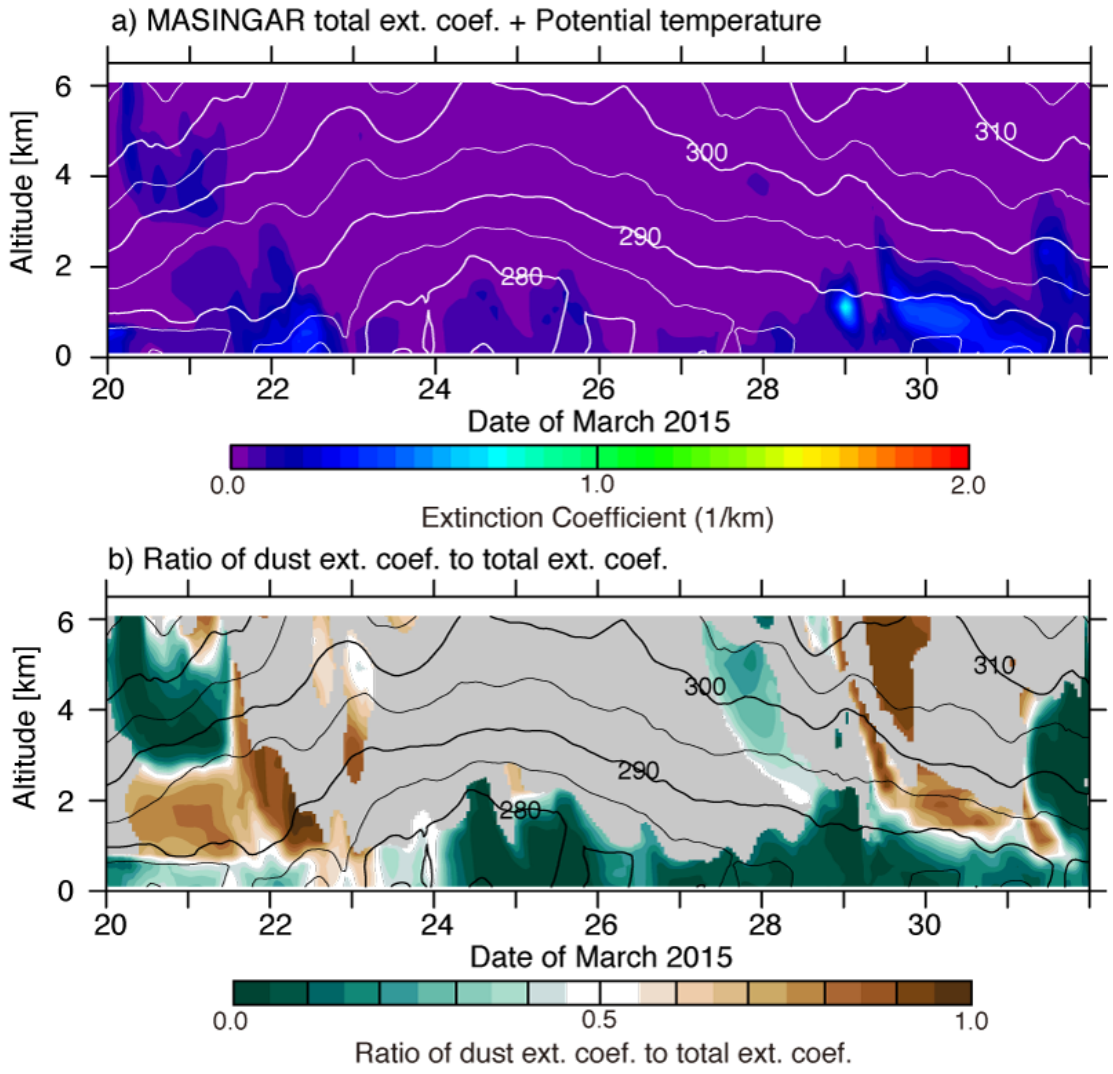

Figure 7. Time (JST)-altitude cross sections of (a) total aerosol extinction coefficients at 550 nm (color shading) and (b) ratios of dust extinction coefficient to total aerosol extinction coefficient (color shading) simulated by the MASINGAR-mk2 with potential temperatures (black contours) over Saga for 20–31 March 2015. The gray regions in Fig. 7b indicate that the simulated total aerosol extinction coefficient was less than 0.02.

(a)

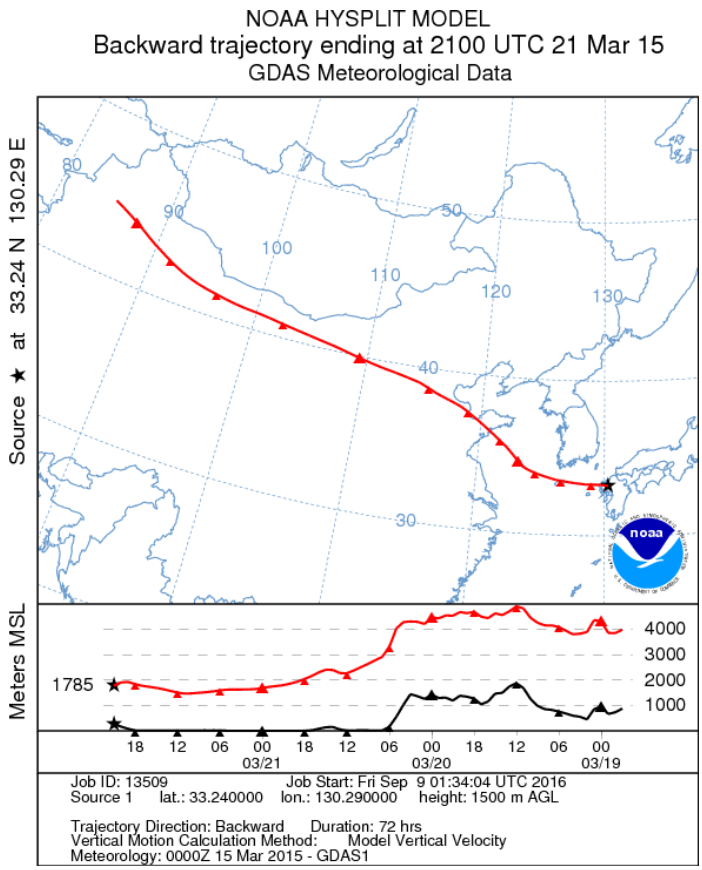

(b)

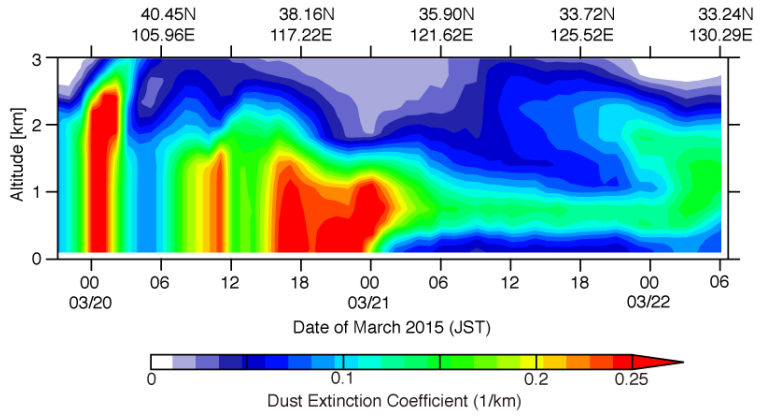

Figure 8. (a) The 72-h HYSPLIT-model backward trajectory (red line) and terrain height (black line) from Saga at 1500 m above ground level (AGL) ending at 06:00 JST on 22 May 2015. (b) Time-altitude cross section of dust extinction coefficient simulated by the MASINGAR mk-2 along the trajectory path.

841 (a)

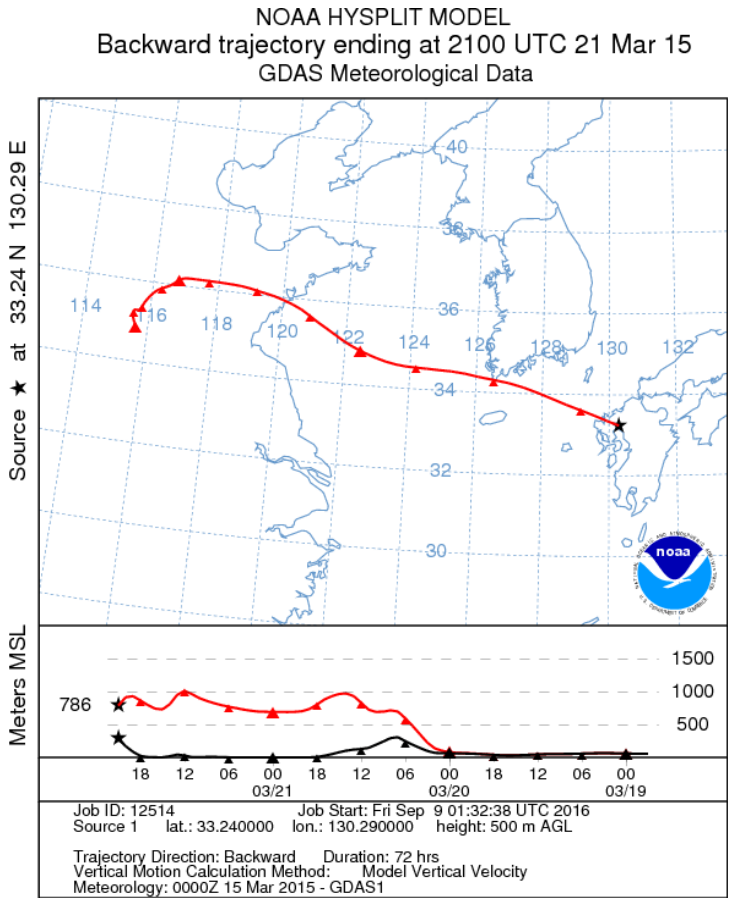

842

843

844 (b)

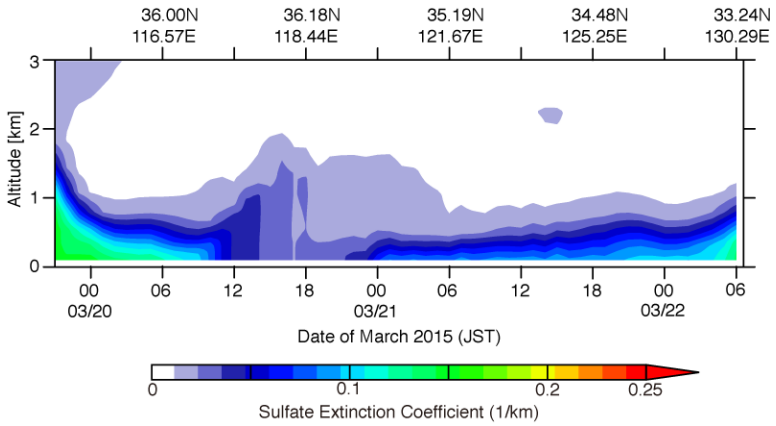

845

846

847 **Figure 9.** Same as Fig. 8, but for AGL at 500 m.

848

849

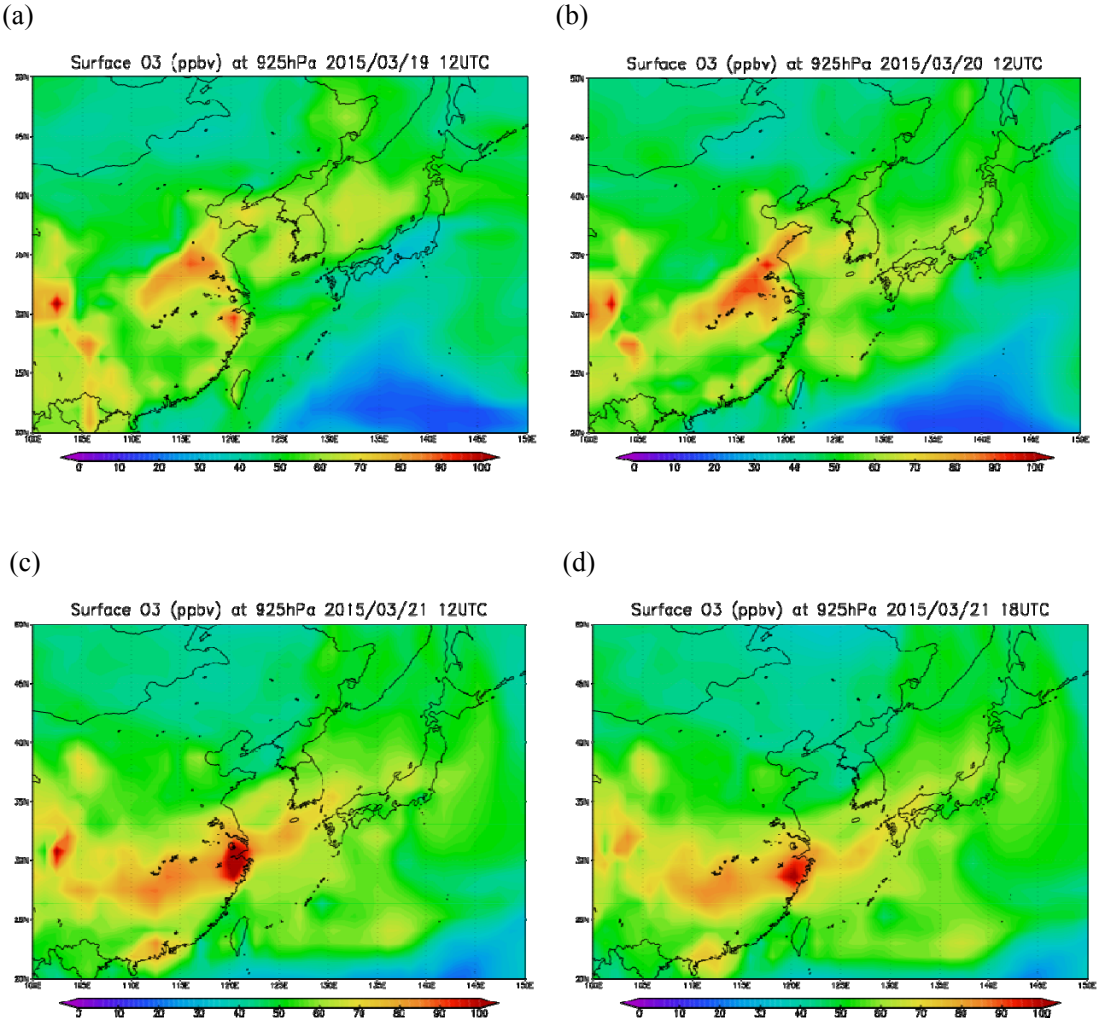

Figure 10. Horizontal maps of ozone volume mixing ratios in ppbv predicted by the MRI-CCM2 for the 925 hPa pressure level (an altitude of about 760 m) at 21:00 JST (JST = UT + 9) on (a) 19, (b) 20, (c) 21 March, and (d) 03:00 JST on 22 March 2015.

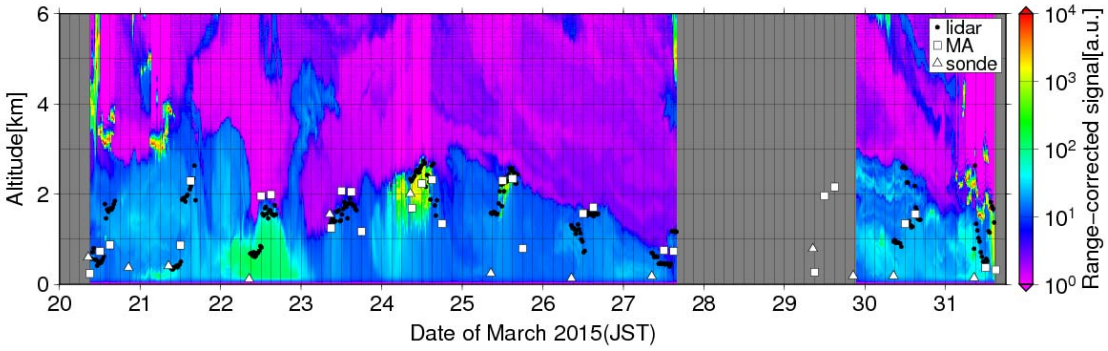

Figure 11. Time-altitude cross section of range-corrected backscatter signal at 1064 nm (color shading) and the heights of the mixed layers estimated by Mie lidar (closed black circles), radiosonde (open triangles), and JMA Meso-Scale Meteorological Analysis (open squares) data over Saga from 09:24 JST on 20 March to 14:34 JST on 31 March 2015.